Joint Geometry and Readout Design for Additively Manufactured Dual-Sensing-Mode Smart Insoles

Marco Torge Gabrecht
Technical University of Applied Sciences Lübeck
Lübeck, Germany
Fraunhofer IMTE
Lübeck, Germany
marco.gabrecht@th-luebeck.de

Ruben Schlonsak
Department of Electrical Engineering and Computer Science
Technical University of Applied Sciences Lübeck
Lübeck, Germany
Fraunhofer IMTE
Lübeck, Germany
ruben.schlonsak@th-luebeck.de

Franziska Seidensticker
Technical University of Applied Sciences Lübeck
Lübeck, Germany
Fraunhofer IMTE
Lübeck, Germany
franziska.seidensticker@imte.fraunhofer.de

Pascal Stagge
Fraunhofer IMTE
Lübeck, Germany
pascal.stagge@imte.fraunhofer.de

Xiangyu Luo
Technical University of Applied Sciences Lübeck
Lübeck, Germany
East China University of Science and Technology
Shanghai, China
xiangyu.luo@stud.th-luebeck.de

Denys J.C. Matthies
Technical University of Applied Sciences Lübeck
Lübeck, Germany
Fraunhofer IMTE
Lübeck, Germany
denys.matthies@th-luebeck.de

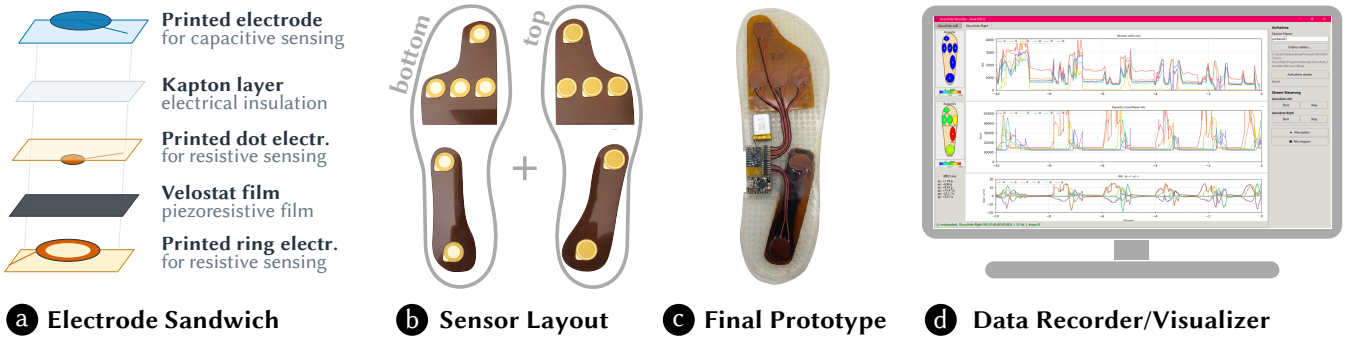


Figure 1: a) Multi-modal pressure sensor: resistive sensing is realized via an inner printed circle electrode and an outer printed ring electrode, which pass current through the pressure-sensitive Velostat film. In alternation, a capacitive mode measures the charging time of the top electrode. b) The sensor insole is produced from two prints that are flipped onto each other. c) In the final prototype, an ESP32 transmits the sensor data, including IMU data, via Bluetooth to a computer. d) The data is visualized and recorded with custom Java software.

Abstract

This paper reports a joint-design fabrication style and laboratory characterization of additively manufactured, dual-mode pressure sensors (resistive + capacitive) for smart insoles. The electrodes are inkjet-printed on a Kapton carrier with a Nano Dimension DragonFly IV and use a manually inserted Velostat film as the piezoresistive element. A systematic screen of 20 ring–circle electrode geometries was used to address a base-resistance limitation of large opposing-plate electrodes, whose low unloaded resistance drives the readout voltage divider toward saturation: geometrically separating an outer ring and a central circle forces a lateral current path through the film and raises the unloaded resistance. Two contrasting candidates, C1R4 and C12R1, were printed at nominal heights from 0.1 to 0.7 mm; the 0.7 mm prints delaminated, whereas all specimens from 0.1 to 0.5 mm remained functional after three-point bending and showed no catastrophic delamination; minor edge cracking was observed at 0.5 mm. A nominal printed height of 0.2 mm is adopted as a fabrication compromise. The two candidates could not be brought into readout range with the same assembled

This work is licensed under a Creative Commons Attribution 4.0 International License.

SCF '26, Tokyo, Japan

© 2026 Copyright held by the owner/author(s).

ACM ISBN 979-8-4007-2821-1/2026/12
https://doi.org/10.1145/3828611.3845657

stack. C12R1 required a folded film with a paper interlayer and C1R4 did not, so the response-versus-stability contrast we report is between assembled configurations and is not attributed to electrode geometry alone. In our final insole prototype, six C1R4 sensors were integrated into a flexible six-zone insole with an ESP32-S3 readout that provides a resistive channel and a capacitive channel per site. Two system recordings show uninterrupted interleaved acquisition, and expose a fixed reference resistor that clips five of six resistive channels against one or other ADC rail, together with an unloaded-resistance spread of more than two orders of magnitude across six nominally identical printed sites. The reported evidence is laboratory characterization of fabricated sensors, not a gait study or a medical-device evaluation.

CCS Concepts

• **Computer systems organization → Embedded systems**; • **Applied computing →** *Health informatics*; • **Computing methodologies → Computational fabrication**.

Keywords

sensor manufacturing, plantar pressure sensor, piezoresistive sensor, capacitive sensor, Velostat, additive manufacturing, 3D-printed electronics, shoe insole, sensor fusion, wearable medical technology

ACM Reference Format:
Marco Torge Gabrecht, Ruben Schlonsak, Franziska Seidensticker, Pascal Stagge, Xiangyu Luo, and Denys J.C. Matthies. 2026. Joint Geometry and Readout Design for Additively Manufactured Dual-Sensing-Mode Smart Insoles. In *Proceedings of the 11th ACM Symposium on Computational Fabrication (SCF '26), December 06–08, 2026, Tokyo, Japan.* ACM, New York, NY, USA, 17 pages. https://doi.org/10.1145/3828611.3845657

1 Introduction

As demonstrated by Bae et al. [2025] and Wade et al. [2025], additive manufacturing enables the simultaneous deposition of conductors, dielectrics, and structural materials within a shared geometry. This capability lets sensing structures become part of the fabricated object rather than externally attached components [Bae et al. 2025; Rasch et al. 2023]. At the same time, it couples design decisions that are largely separable in conventional electronics. Changing a printed electrode may alter the current path, contact area, mechanical flexibility, solder-joint loading, readout range, and interference with a second sensing modality. A design optimized for an isolated metric before fabrication may therefore fail after assembly or connection to its acquisition hardware [Schmitz et al. 2017].

Developing custom plantar-pressure sensors provides a concrete example, because feet differ per user and the sensing surface has to be manufactured to fit. The long-term goal of the wider research project is a tool that supports diagnosis and monitoring of diabetic foot syndrome (DFS), a complication in which peripheral neuropathy removes protective sensation so that sustained pressure points and microtrauma go unnoticed [Armstrong et al. 2023], peripheral arterial disease impairs wound healing through restricted microcirculation [Fowkes et al. 2013], and diabetes-related gait changes concentrate plantar load into local peaks that raise ulceration risk [Fernando et al. 2013; Tsaklis and Tentolouris 2018]. The burden is substantial. In Germany an estimated 550,000 to 850,000 people require treatment for DFS, and five-year mortality after a diabetes-related amputation is on the order of 50% [Hochlenert 2024; Morbach et al. 2022]. That burden is why continuous measurement of plantar loading is an attractive long-term target [Castro-Martins et al. 2024; Saeedi et al. 2019] and why practical non-invasive systems for daily-life monitoring remain an open problem [Bus and van Netten 2016; Latsch et al. 2026].

We state at the outset what that motivation does and does not license here. Existing insole systems employ resistive, capacitive, optical, and piezoelectric transduction, and reviews of this literature recur on five open challenges: calibration, hysteresis, durability, sensor placement, and system integration [Abdul Razak et al. 2012; Castro-Martins et al. 2024; Latsch et al. 2026]. This paper works on two of them. Sensor placement enters as a hard geometric constraint that shapes the electrode family, and system integration is the subject of the six-zone implementation and of the failure modes we measured in it. Calibration, hysteresis, and durability are *not* addressed: neither channel is calibrated to absolute pressure, hysteresis is not quantified, and the bending experiments are short-cycle stability tests, not fatigue tests. Those three we return to as future work. The evidence reported here is a laboratory characterization of fabricated sensors. It is not a gait study, not a medical-device evaluation, and involves no participants. What DFS supplies is the set of requirements that constrain the design (thin and flexible structures, distributed sensing sites, mechanically stable electrical connections, and useful response across changing load conditions), not a claim about clinical performance.

In this paper, we present an artifact that combines inkjet-printed silver and dielectric structures with a manually inserted Velostat film. Its resistive electrodes form a non-overlapping ring and circle, so the printed geometry defines a lateral current path through the film. A separate, electrically isolated printed conductor provides a capacitive channel, read as the ESP32-S3 self-capacitance. We did not include a matched opposing-plate control or absolute-pressure calibration; our evaluation concerns the fabricated ring–circle family and its readout constraints.

This framing places the work squarely in computational fabrication: the object of study is not a sensor in isolation but the joint design space of printed geometry, assembled stack, and readout circuit. Because inkjet printing lets a single geometry parameter move electrode area, current path, mechanical stiffness, and solder-pad loading at once, decisions that a conventional design flow would separate must here be made together and judged after assembly. Our contribution is to make that coupling explicit for one concrete family and to report where it helps, where it constrains the readout, and where it fails.

We therefore ask: *What electrical response and short-bending stability trade-offs emerge among contrasting members of a parametric ring–circle current-path family, and what fabrication and readout constraints govern their integration into a dual-mode pressure-sensing artifact?* We address this question by fabricating 20 electrode geometries, characterizing two contrasting selected candidates, testing a series of nominal printed heights, and analyzing a six-zone acquisition implementation.

The measurements do not identify a universal optimum but show different outcomes across metrics. The configuration built around a large central electrode (C12R1) has the larger clamp response,

whereas the configuration built around a small center and wide ring (C1R4) has the more stable signal and a substantially smaller post-bending change in the pressure–resistance curve minimum. We write *configuration* deliberately: the two candidates required different Velostat stacks, so the contrast does not isolate electrode geometry. What the comparison does support is the computational-fabrication view that printed geometry is an electrical and system variable and not only a shape variable. Considering clamp response, constant-load stability ratio, post-bending change, and the simpler assembled stack, C1R4 is the system-specific choice; the six-zone implementation uses it despite C12R1's larger clamp excursion.

In addition to the final insole artifact, the paper makes three contributions:

- A 20-member parametric ring–circle electrode family that uses geometric separation to define a lateral current path through a piezoresistive layer, with two contrasting candidates retained for focused study.
- An evaluation of geometry screening, printed-height bending (0.1–0.5 mm), constant-load stability ratio, and short bending. It reveals a configuration-level response-versus-stability pattern, and states explicitly which part of that pattern the experiment cannot attribute to geometry alone.
- A six-zone dual-mode Prototype 4 using C1R4, whose recordings show uninterrupted interleaved acquisition and no recurrence of the shared-conductor failure, and which exposes two readout-side results: reference-resistor-limited clipping at *both* ADC rails, and an unloaded-resistance spread of more than two orders of magnitude across six nominally identical printed sites of a single device.

Scope and limitations. The geometry–height series used one specimen per condition, and specimen identity was not tracked consistently across the focused electrical tests, so the reported differences describe C1R4 and C12R1 as fabricated in this study, not independent effects of circle diameter or ring width. The two focused candidates were assembled with different Velostat stacks, and the response-versus-stability contrast cannot be separated from that difference. The bending protocol comprises two 10-min exposures with unrecorded cycle counts, so it characterizes short-cycle electrical stability, not durability. Neither channel is calibrated to absolute pressure, and the six-zone recordings have no synchronized force or location ground truth; they characterize acquisition behavior and per-site working points, not sensing accuracy. Section 7 develops each of these.

2 Related Work

2.1 Fabricated Plantar-Pressure Systems

Plantar-pressure systems differ in transduction method, number and placement of sensing sites, calibration, footwear integration, and acquisition hardware. Reviews by Abdul Razak et al. [2012], Castro-Martins et al. [2024], and Latsch et al. [2026] show both the range of available approaches and the absence of a single architecture that dominates across flexibility, spatial coverage, repeatability, and long-term wear. These reviews also note recurring trade-offs: resistive elements are simple and robust at high load but drift and show hysteresis, whereas capacitive elements resolve light load well but are sensitive to electromagnetic interference and to the mechanical details of the dielectric [Grosse-Puppendahl et al. 2017; Matthies et al. 2013]. Combining modalities is a common response, and the fabrication method increasingly determines how well two transducers can be co-located in one thin, flexible site.

Table 1: Transduction principles for plantar-pressure and tactile sensing, compared on the axes that constrain a thin, area-limited, printable site. "Per-site part" asks whether the principle needs a discrete component at every sensing location beyond the printed layers themselves.

Principle	Main limitation	Static load	Per-site part
Resistive [Giovanelli and Farella 2016]	drift, hysteresis	yes	no
Capacitive [Samarentsis et al. 2022]	EMI, dielectric detail	yes	no
Piezoelectric [Abdul Razak et al. 2012]	responds to change only	no	no
Optical [Leal-Junior et al. 2019]	source/detector at boundary	yes	yes
Magnetic [Peng et al. 2025]	magnet plus rigid die, ferromagnetic interference	yes	yes

Fabrication has increasingly become part of insole customization. Samarentsis et al. [2022] printed a capacitive smart insole; Aqueveque et al. [2018] used a flexible-PCB capacitive array; Tao et al. [2020] controlled dielectric pore geometry for real-time pressure mapping; Leal-Junior et al. [2019] used 3D-printed polymer optical fibers for plantar force monitoring; and Gabrecht et al. [2023] 3D-printed a flexible pneumatic insole system to detect pressure changes. These systems demonstrate that manufacturing method and transducer geometry can shape the sensing function. Table 1 summarizes how the transduction principles used in insole and tactile sensing differ on the axes that matter for a printed, thin, area-constrained site. Piezoelectric elements respond only to load *changes* and cannot report a static pressure, which rules them out for standing-load monitoring. Optical fiber approaches avoid electrical interference entirely but need a light source and detector at the boundary of the insole [Leal-Junior et al. 2019]. Magnetic transduction (Hall-effect, magnetoresistive, or magnetoelastic) offers large dynamic range, genuine multi-axis force sensing, and immunity to contact-resistance drift, but requires a permanent magnet or magnetized elastomer at every site together with a rigid sensing die, and is sensitive to nearby ferromagnetic material [Peng et al. 2025]. For the present device the deciding constraint is the one in Section 3.1: the site must stay inside roughly 18 mm and remain printable in the same pass as the rest of the insole, which favors the resistive/capacitive pair and disfavors any principle needing a discrete component per site. This is a selection argument for this application, not a general ranking.

Our focus is narrower: the fabricated design space of a non-overlapping ring–circle current path and the electrical, mechanical, and integration trade-offs recorded for its implementations.

2.2 Piezoresistive and Dual-Mode Flexible Sensors

Velostat is a carbon-loaded polyethylene composite whose resistance changes with compression and contact conditions [Dzedzickis et al. 2020]. It is accessible for prototyping, but force-sensitive resistors exhibit nonlinear response, hysteresis, drift, and unit-to-unit variation [Giovanelli and Farella 2016]. Models of semiconductive-polymer force sensors describe a force-dependent resistance and the influence of the measurement circuit [Kalantari et al. 2012]. Inverse viscoelastic models have also been used to compensate dynamic insole-sensor behavior [Laaraibi et al. 2023]. These properties make the sensor/electronics working point a design constraint, but we do not claim a calibrated material model. For the second modality, self-capacitance readout on a microcontroller touch peripheral is a low-cost route to a capacitive channel without a dedicated analog front end, at the cost of an environment-sensitive count. Prior work has explored hybrid resistive–capacitive stacks [Matthies et al. 2025]. Here, we study their integration into an inkjet-printed ring–circle structure and characterize the resulting fabrication and readout constraints.

Hybrid capacitive–piezoresistive devices combine complementary responses, resistive robustness at high load with capacitive sensitivity at low load, as shown in micropillar-based flexible sensors [Shen et al. 2023; Xiao et al. 2026]. Our sensor likewise provides two channels: a force-dependent resistive path through Velostat and a capacitive channel formed by a separate printed electrode and read as the ESP32-S3 self-capacitance through the `touchRead()` peripheral. We refer to this as a *dual-mode* sensor. The two channels show different pressure-response ranges in the focused prototype measurements; a dedicated sensor-fusion algorithm is left to future work.

2.3 Computational Fabrication of Sensing Structures

Prior computational-fabrication research has integrated functional materials, sensors, and fabrication-aware geometry. MultiFab coordinated multiple materials and machine vision in one platform [Sitthi-Amorn et al. 2015]. Capricate exposed a pipeline for placing printed capacitive touch sensors in interactive objects [Schmitz et al. 2015]; Steel-Sense integrated mechanical elements and sensing through additive manufacturing [Vasilevitsky and Zoran 2016]; and Hagino et al. [2017] addressed electrode placement on printed surfaces at SCF. Broader reviews describe both the design opportunity and manufacturing limits of 3D-printed electronics [Khosravani and Reinicke 2020; Tan et al. 2022].

Closest to our own question, two lines of work make printed geometry the functional variable. Yu et al. [2024] tuned the infill pattern and density of a fused-deposition print to set the response of a 3D-printed pressure sensor, varying an internal geometric parameter to move the mechanical and electrical behavior of the finished part. Watschke et al. [2021] used additive-manufacturing geometry to shape a resistive sensor's current path. Our contribution sits alongside both: where Yu et al. vary internal infill and Watschke et al. shape the path in a single-mode resistive element, we vary a planar electrode outline and carry the consequences through to a dual-mode readout and a six-site integration. This is neither a new printer nor a general-purpose CAD system, but a fabrication and characterization study of geometry-defined current paths.

3 Sensor Design

3.1 Design Constraints and Base-Resistance Motivation

Two constraints shaped the electrode design before any electrical optimization. First, the same printed layout must serve the full target range of shoe sizes (EU 38–46) without mechanical modification, which places opposing requirements on sensor size: each site must be large enough for adequate active area and signal-to-noise ratio, yet small enough to fit the narrowest forefoot. We treated the ability to place three sensors side by side across the metatarsal region, where the highest plantar pressures occur during push-off [Latsch et al. 2026; Tsaklis and Tentolouris 2018], as the limiting geometric criterion, which fixes the outer electrode diameter at roughly 18 mm. The six sites comprise the hallux, the first, third, and fifth metatarsal heads, the midfoot, and the heel. The hallux, heel, and metatarsal heads follow clinically established high-pressure regions of the diabetic foot [Castro-Martins et al. 2024; Fernando et al. 2013].

Second, the earlier opposing-plate prototypes exposed a readout limitation rather than a transduction failure. For two large plates of area A separated by a thin Velostat film of thickness d, the unloaded resistance scales as

$$R_0 \propto \frac{d}{A}, \tag{1}$$

so a large overlapping area yields a low R_0 that drives the voltage divider of Equation (3) toward its rail before any load is applied, compressing the usable range. Because the Velostat resistance follows an approximate power law in force,

$$R_s(F) = k\,F^{-n}, \tag{2}$$

the working point is effectively set on a logarithmic resistance scale [Kalantari et al. 2012], and an unfavorably low R_0 cannot be recovered by the reference resistor alone. Forcing current to travel laterally through the film between two non-overlapping regions, instead of straight across a wide overlap, raises R_0. This motivates the ring–circle family developed next, which follows the principle of geometry-shaped current paths in additively manufactured resistive sensors [Watschke et al. 2021].

3.2 Parametric Ring–Circle Electrode Family

The core design family pairs two non-overlapping conductive patterns on opposite sides of the Velostat: an outer ring and a central circle. The outer ring diameter remains 18 mm. Four factorial ring widths (1–4 mm) were combined with four circle diameters (1, 3, 5, and 9 mm); four additional center or large-circle conditions brought the screen to 20 geometries. Each design is denoted CxRy, where x is circle diameter and y is ring width in millimeters.

Because the two conductive regions do not overlap, current must enter the pressure-sensitive sheet at one region, traverse a lateral portion of the sheet, and exit through the other. Varying the inner circle and outer ring therefore changes electrode area, gap, and candidate current paths together. This is a design hypothesis rather than a spatial current-density measurement; the experiment tests its observable electrical consequences.

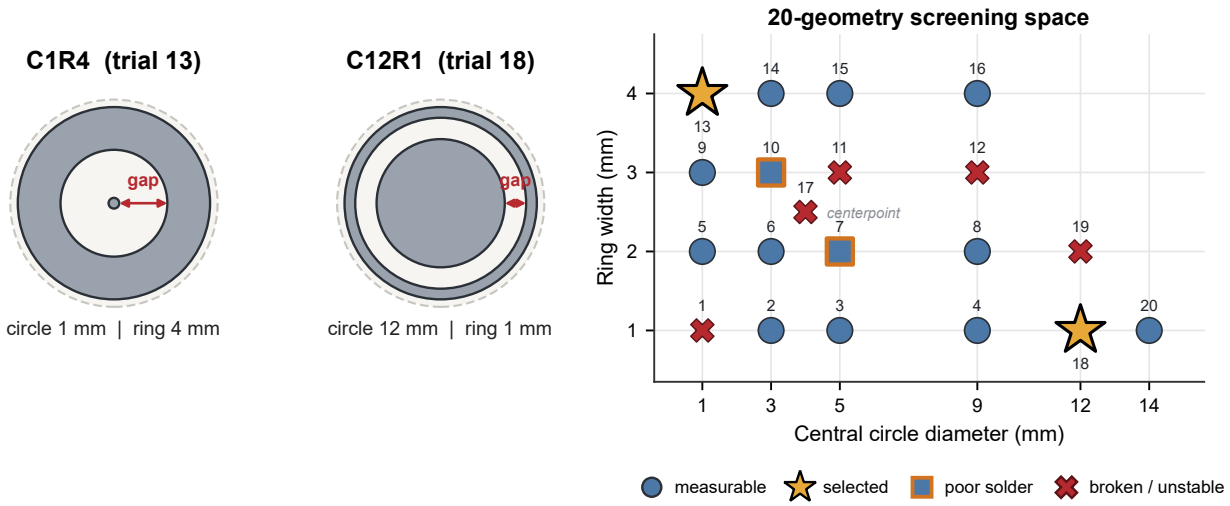


Figure 2: Parametric ring–circle family. Left: schematics of the two retained contrasting candidates (C1R4 and C12R1), with arrows indicating their electrode gap. Right: the complete 20-geometry screening space (central circle diameter versus ring width), with measurable, poor-solder, broken/unstable, and selected candidates marked; trial 17 is the factorial centerpoint.

Within this family we distinguish two sub-types by which electrode carries the small counter-area. In a *circle-type* layout the counter-electrode is the central circle and current spreads radially inward from the surrounding ring; in a *ring-type* layout the counter-electrode is a narrow outer ring and current spreads radially outward from a broad center. Both realize the same principle: a small counter area forces a longer lateral path and higher unloaded resistance. However, they distribute contact pressure and current density differently. This is one reason why the screen varied the diameter of the circle and the width of the ring jointly rather than independently. C1R4 (a small center with a wide ring) and C12R1 (a large center with a narrow ring) sit at opposite corners of this sub-type space, and were retained as contrasting candidates for exactly that reason.

Figure 2 shows the complete screen. C1R4 (trial 13) has a 1 mm circle, a 4 mm ring, and a source-reported ring-to-circle area ratio of 221.5. C12R1 (trial 18) has a 12 mm circle, a 1 mm ring, and a reported area ratio of 0.47. These two contrasting layouts were retained because both had measurable resistance and supported focused follow-up. After the subsequent electrical and bending evaluations were considered, C1R4 was selected for further smart-insole development; this choice does not make it a universal geometric optimum. Trial 20 extends to a larger 14 mm circle and marks the geometric boundary of the screen.

Table 2 lists the complete screen: every trial with its unloaded resistance R_0, its resistance under body-weight load, its resistance under the XC7 clamp, and the fabrication outcome where a coupon could not be measured. Across the family, the ring–circle geometry raises R_0 well above the opposing-plate baseline (from single-digit to tens of kΩ), which is the effect the lateral current path was intended to produce.

3.3 Dual-Mode Layer Stack and Readout Principle

The six-zone implementation is not a single parallel-RC element. Its two observables originate from galvanically isolated conductors: a force-dependent resistive path through Velostat and a load-dependent capacitance at a separate ESP32-S3 capacitive electrode. They are mechanically coupled through the common stack and applied load, but they are not separated from one shared impedance at a corner frequency.

For resistive measurement, a printed circle and ring contact opposing sides of Velostat. With the sensor as the lower arm of a voltage divider, the ideal ADC input is

$$V_{\mathrm{ADC}}(F) = V_{\mathrm{s}} \frac{R_{\mathrm{s}}(F)}{R_{\mathrm{ref}} + R_{\mathrm{s}}(F)}. \tag{3}$$

Thus, sensor resistance far above or below R_{ref} drives the readout toward the upper or lower ADC rail, respectively. Compression changes the material and interface resistance. The single-channel characterization circuit used a 2.7 kΩ fixed resistor, whereas the six-zone divider uses $R_{\mathrm{ref}} = 4.7\,\mathrm{k\Omega}$ and records raw 12-bit ADC counts. The six-zone stack uses C1R4 with unfolded Velostat and no paper interlayer. C12R1 produced an unfavorable divider ratio at the intended readout. To obtain a usable working point, the Velostat had to be folded and a paper interlayer placed between the folds. C1R4 has so far required neither modification. The divider should still be designed around the measured resistance interval. A common log-symmetric rule is

$$R_{\mathrm{ref}} = \sqrt{R_{\mathrm{min}} R_{\mathrm{max}}}, \tag{4}$$

which centers the geometric resistance range. Equation (4) follows directly from the power-law response of Equation (2): because resistance moves multiplicatively with force, the divider is best centered on the geometric mean of R_{min} and R_{max} rather than their

Table 2: Complete 20-geometry screen (ring width and circle diameter in mm; all resistances in kΩ). R_0 is the unloaded resistance, R_{body} the resistance under body-weight load (63-kg research-team member, standing), and R_{clamp} the resistance under the Bessey XC7 spring clamp. Trial 13 is C1R4 and trial 18 is C12R1; trial 17 is the factorial centerpoint. Five coupons were broken or electrically unstable and two more failed at the manual solder joint; those outcomes are listed, not omitted. All values are source-reported single measurements, given to bound the manufacturable range and not to rank geometries quantitatively.

#	Type	Ring	Circle	R_0	R_{body}	R_{clamp}	Note
1	Circle	1	1	unstable	–	–	too small
2	Circle	1	3	5.4	3.9	2.6	
3	Circle	1	5	2.7	1.3	1.35	
4	Circle	1	9	3.3	0.72	1.3	bottleneck
5	Circle	2	1	28	2.2	2.4	large R_0
6	Circle	2	3	6.0	1.8	2.5	
7	Circle	2	5	2.1	1.13	1.66	poor solder
8	Circle	2	9	4.4	0.84	0.6	
9	Circle	3	1	4.4	2.02	2.6	
10	Circle	3	3	10.3	7.21	7.1	poor solder
11	Circle	3	5	broken	–	–	
12	Circle	3	9	broken	–	–	
13	**Circle**	**4**	**1**	**20**	**11**	**13**	C1R4
14	Circle	4	3	11	8.54	1.2	
15	Circle	4	5	2.0	0.73	0.76	
16	Circle	4	9	1.7	0.07	0.8	min. gap
17	Circle	2.5	4	broken	–	–	centerpoint
18	**Ring**	**1**	**12**	**9.0**	**0.91**	**1.3**	C12R1
19	Ring	2	12	broken	–	–	
20	Ring	1	14	5.7	1.24	1.1	max. circle

arithmetic mean, which would bias the working point toward high resistance and reach the ADC rail prematurely.

From top to bottom, the stack is Kapton, dielectric, isolated capacitive electrode, dielectric separator, resistive circle, unfolded Velostat, resistive ring/counter-electrode, dielectric, and Kapton; it contains no paper interlayer (Table 3). The intermediate dielectric (layer 4) keeps the capacitive conductor and the resistive path galvanically separated, an arrangement adopted specifically to remove the conductor sharing described below. The ESP32-S3 touch peripheral reads the self-capacitance of the isolated electrode, which increases as load compresses the stack and changes its effective geometry and permittivity, following the parallel-plate relation

$$C = \frac{\varepsilon_0 \, \varepsilon_r \, A}{d}. \tag{5}$$

We report this capacitive channel as raw counts, not calibrated capacitance.

3.4 Prototype Iteration

The six-zone artifact is the fourth in a sequence of prototypes whose limitations were largely fabrication- and readout-driven; we summarize the earlier three because they motivate both the ring–circle geometry and the galvanic separation used here.

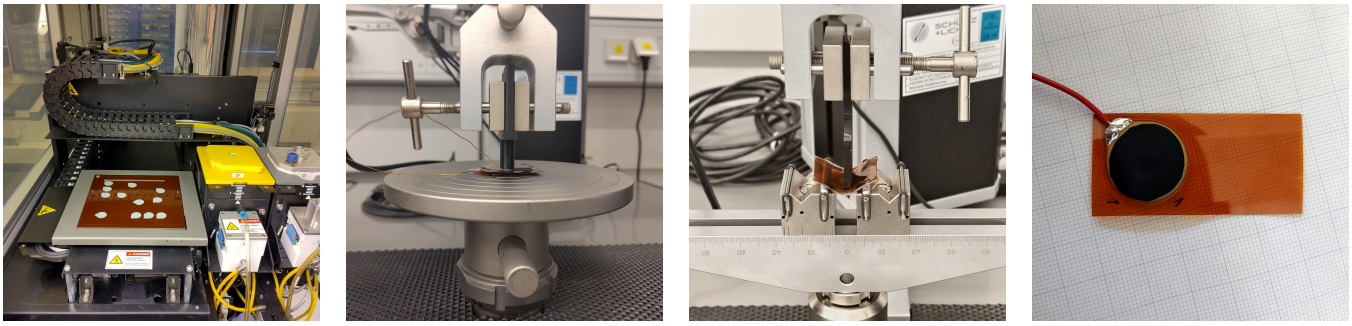
Table 3: Layer stack of the galvanically separated six-zone sensor (top to bottom). Layer 3 (capacitive electrode) connects only to touch GPIOs; layer 7 serves only the resistive current path; layer 4 keeps the two paths isolated. No paper interlayer is used.

#	Material	Function	Connection
1	Kapton film	Carrier / insulation (top)	–
2	Dielectric ink	Insulation	–
3	Conductive ink	Capacitive electrode	ESP32-S3 touch GPIO
4	Dielectric ink	Isolation of layers 3/5	–
5	Conductive ink	Resistive electrode (circle)	Divider / ADC GPIO
6	Velostat	Piezoresistive element	–
7	Conductive ink	Ring / counter-electrode	GND
8	Dielectric ink	Insulation	–
9	Kapton film	Carrier / insulation (bottom)	–

Prototype 1 (proof of concept). Prototype 1 verified that a single printed stack can expose both a force-dependent resistance and a capacitive observable, using a planar parallel-electrode layout, an Arduino Nano, and a 10 kΩ adjustable reference resistor. Both observables responded to applied pressure, but the layout was too small for reliable manual soldering, and soldering temperatures delaminated the printed electrodes, forcing a redesign. It also set the two questions that recur through the later prototypes: whether a printed pad can carry a reliable manual solder joint, and whether the base resistance sits where the divider can use it.

Prototype 2 (sizing and noise). Prototype 2 used circular parallel-plate electrodes of 5, 10, 15, 20, and 30 mm diameter and moved the readout to an ESP32-S3. The reference resistor was reduced from 10 to 1 kΩ after the divider saturated above ≈ 20 N, an early symptom of the base-resistance problem later addressed geometrically (Equation (1)). Load tests on a Galdabini Quasar 100 confirmed a measurable response up to 900 N, above the ≈ 785 N static weight of an 80 kg person [Tsaklis and Tentolouris 2018]. The 5 and 10 mm electrodes shorted under load and could not be measured; sizes ≥ 15 mm produced usable qualitative pressure response, and the SNR at 200 N was quantified for the 20 and 30 mm candidates that also met the side-by-side forefoot constraint (Table 4), with the capacitive channel read through the ESP32 touch peripheral. The size sweep also fixed the noise protocol used afterward: a 30 s unloaded recording characterized the noise floor and a 120 s recording at 200 N characterized the loaded signal, from which the ratios in Table 4 were computed. The 30 mm electrode gave the highest capacitive SNR, but the side-by-side forefoot constraint capped the usable diameter, so 20 mm was retained as the compromise.

Prototype 3 (shared-electrode integration). Prototype 3 integrated six sensors of the selected ring–circle geometry into a first flexible insole but retained a lower counter-electrode shared between the resistive and capacitive paths at each site, with the resistive channel read through the ESP32-S3 LEDC + DMA-ADC and the capacitive channel through the internal touch peripheral. Bench recordings showed severe crosstalk: the capacitive channel froze while the resistive excitation ran and produced abrupt recovery artifacts after each phase change, and the resistive channel showed



(a) DragonFly print bed (b) Compression fixture (c) Three-point bending (d) Assembled sensor

Figure 3: Fabrication and evaluation apparatus. The sensor sheet is printed on Kapton (a); a universal testing machine applies compression (b) and three-point bending (c); an assembled ring–circle sensor shows the Velostat and wired printed sensor (d).

periodic dropouts coinciding with the capacitive charge-transfer cycles; neither channel yielded usable data. We attribute this to the shared ground coupling the two paths. The 100 kHz resistive excitation creates transients on the common ground, which disturb the capacitive charge-transfer measurement. Meanwhile, the capacitive electrode's discharge feeds back into the resistive divider. Full galvanic separation, implemented by the Prototype 4 stack in Table 3, is the corrective measure. The six-zone results evaluate whether the specific frozen capacitive output and periodic resistive dropouts recur. Prototype 3 shows how saving one printed layer by sharing a conductor can prevent the two readouts from operating together at the same site.

3.5 Six-Zone Dual-Mode Implementation

The six-zone implementation is Prototype 4, the galvanically separated successor to Prototype 3. The insole uses C1R4 at six sites: the hallux (S1), first, third, and fifth metatarsal heads (S2–S4), midfoot (S5), and heel (S6). An ESP32-S3 reads six resistive ADC inputs and six capacitive inputs. A scheduler alternates the two modes on a fixed 20-ms tick, so resistive and capacitive samples are never taken at the same time; each channel is sampled at a nominal 25 Hz per mode. Each BLE packet carries the twelve raw counts and a sample index, and the data were recorded without calibration or classification. Interleaving the modes and separating the electrodes galvanically together prevent the charge-transfer interference observed in Prototype 3. Tests 3 and 4 evaluate this configuration.

Table 4: Prototype 2 raw-output SNR at 200 N constant load. The capacitive channel was read through the ESP32 touch peripheral. The 5 and 10 mm electrodes shorted under load; SNR is reported for the 20 and 30 mm candidates.

Diameter	Channel	SNR (dB)
20 mm	Capacitive	34.84
20 mm	Resistive	32.60
30 mm	Capacitive	65.47
30 mm	Resistive	36.61

4 Experimental Characterization

Figure 3 shows the fabrication and test equipment. Two loading instruments were used (Figure 3b,c). Repeatable static clamp conditions (identified as XC3, XC5, and XC7) were applied with Bessey Clippix XC spring clamps [Bessey GmbH & Co. KG 2022], which give a fixed, hands-free clamp force convenient for screening and constant-load noise measurements. Controlled compression and three-point bending used a Galdabini Quasar 100 universal testing machine [Galdabini S.p.A. 2021]; for the lower-force pressure and bending measurements, its 100 kN load cell was replaced with a 1 kN cell to improve force resolution. Body-weight reference resistances (R_{body} in Table 2) were recorded with a 63 kg member of the research team standing on the sensor as a single mechanical screening condition.

4.1 Geometry Screening

Each ring–circle pair was measured unloaded and under a Bessey XC7 spring clamp. Two terms recur throughout the paper for this measurement. The *clamp reduction* is the relative drop in resistance from the unloaded value R_0 to the value R_{clamp} under a named clamp, $(R_0 - R_{\text{clamp}})/R_0$, given as a percentage. The *clamp response* is that same drop read as a response amplitude, so the geometry with the larger clamp reduction is the one with the larger clamp response. Both refer to one static loading condition set by the spring clamp, and neither is a calibrated pressure sensitivity. C1R4 changed from 20 kΩ unloaded to 13 kΩ under the XC7, a 35.0% reduction. C12R1 changed from 9 kΩ to 1.3 kΩ, an 85.6% reduction. Five candidates were broken or unstable and two additional candidates were flagged for poor soldering. Figure 2 includes these failures. Beyond the two retained candidates, the screen served mainly to bound the manufacturable region: designs with a very small counter-area were electrically unstable, designs with near-total overlap gave a low R_0 and a poor divider ratio, and several coupons failed at the manual solder joint instead of in the printed structure.

4.2 Printed-Height Characterization

Both designs were printed at eight nominal heights between 0.1 and 0.7 mm (0.10, 0.15, 0.20, 0.25, 0.30, 0.40, 0.50, and 0.70 mm; the series is deliberately finer below 0.3 mm, where the compromise

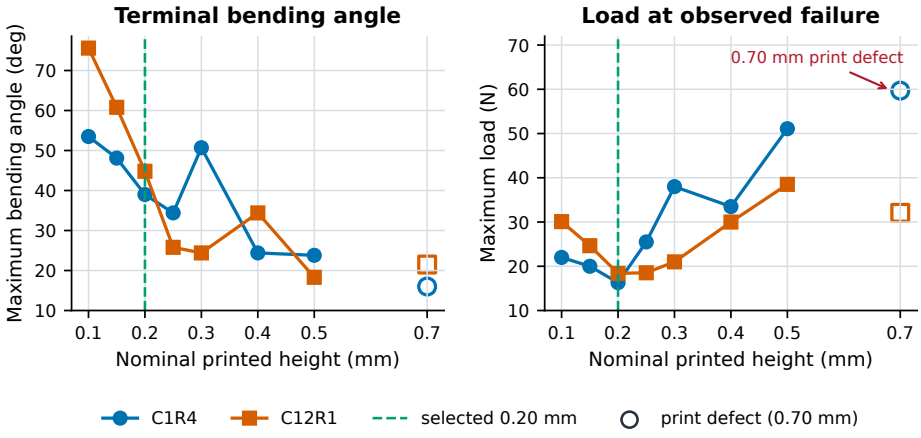


Figure 4: Mechanical height characterization (one specimen per height; terminal angle and load at the end of each non-destructive bending test). Specimens from 0.10 to 0.50 mm remained functional and showed no catastrophic delamination; minor edge cracking was observed at 0.50 mm. The 0.70 mm prints delaminated and are shown as hollow points, unjoined to the characterized series. The dashed line marks the selected 0.20 mm compromise.

was expected); because AgCite® 90072 and Ink 1092 are costly, a single specimen was fabricated per height. The 0.7 mm prints were unusable: the silver layer delaminated, and additional print defects appeared (Fig. 4, hollow points). We tentatively attribute the delamination to thermal residual stress: a coefficient-of-thermal-expansion mismatch between the silver and dielectric inks would produce interfacial shear stress on cooling that grows with layer thickness and, beyond some thickness, exceeds the interfacial adhesion, a mechanism reported for other printed multi-material laminates [Laureto et al. 2017]. We did not measure residual stress or interfacial adhesion here, so this remains a hypothesis consistent with the observed thickness dependence, not a demonstrated cause. Bending characterization was therefore restricted to the 0.1–0.5 mm specimens, each fully assembled with all layers in the final stack to reflect real operating conditions.

A universal testing machine applied three-point bending with a nominal fixture setting of 15 mm. The initial crosshead rate was $2\,\mathrm{mm\,min^{-1}}$. After initial deformation, the rate was $5\,\mathrm{mm\,min^{-1}}$. We recorded the terminal load, displacement, and bending angle reached. All specimens from 0.1 to 0.5 mm remained functional after bending, and both sensing channels still responded. Minor edge cracking appeared at 0.5 mm, but no catastrophic delamination occurred. Table 5 lists the per-height mechanical quantities. We report the apparent terminal stiffness $k_{\mathrm{app}} = F_{\mathrm{term}}/s_{\mathrm{term}}$, a secant ratio evaluated at each specimen's different terminal working point, not a force–deflection slope or flexural modulus. Converting the measurements into a material modulus would also require the specimen width and actual laminate thickness under the indenter, neither of which was recorded per specimen.

Apparent terminal stiffness increased monotonically with nominal printed height for both geometries, from 3.14 to $16.43\,\mathrm{N\,mm^{-1}}$ for C1R4 and from 3.04 to $16.11\,\mathrm{N\,mm^{-1}}$ for C12R1. The values were closely matched from 0.10 to 0.25 mm and again at 0.50 mm, whereas larger between-design differences occurred at 0.30 and 0.40 mm. Terminal load, displacement, and bending angle were not monotonic across neighboring heights. Given the single specimen per condition, the series supports a shared thickness-dependent stiffening trend, but not a geometry-independent stiffness law. For both geometries, k_{app} remained near $3.0\,\mathrm{N\,mm^{-1}}$ to $3.2\,\mathrm{N\,mm^{-1}}$ from 0.10 to 0.20 mm and increased from 0.25 mm onward. This transition is consistent with a substrate-dominated thin regime followed by an increasing contribution of the printed stack, but the single specimens and unmeasured actual laminate thickness preclude a mechanistic conclusion. The 0.2 mm height retains clearly larger bending angles than the thicker conditions (39.0° and 44.8°, against 23.8° and 18.3° at 0.5 mm) while giving more printed and interconnect support than the thinnest parts, whose solder-joint transition acts as a stress concentrator. The result supports 0.2 mm as a pragmatic design compromise on the selected metrics and assembly observations; "optimal thickness" would overstate the evidence.

4.3 Dynamic Pressure Response

Focused pressure-response measurements used separately fabricated nominal 0.2 mm C1R4 and C12R1 prototype specimens with the single-channel readout. C1R4 used unfolded Velostat without a paper interlayer, whereas C12R1 used the folded-film/paper configuration required to place that prototype within the readout range. The comparison therefore concerns the two assembled prototype configurations, not an isolated causal effect of electrode geometry.

For the resistive comparison, the universal testing machine applied the same triangular force profile to each specimen, from nominally zero load to approximately 170 N and back to zero, using a flat disk loading head and a foam layer to distribute load. Resistance and force were recorded over the loading and unloading sequence. We define mean force sensitivity over the loading range as

$$S_R = \frac{\Delta R}{\Delta F}, \tag{6}$$

Table 5: Three-point bending quantities for C1R4 (D13) and C12R1 (D18) across printed heights (non-destructive; terminal load F_{term}, terminal deflection s_{term}, bending angle θ, and apparent terminal stiffness $k_{\text{app}} = F_{\text{term}}/s_{\text{term}}$). The ratio is evaluated at different terminal working points and is not a force–deflection slope or material modulus.

	C1R4 (D13)				C12R1 (D18)			
Height (mm)	F_{term} (N)	s_{term} (mm)	θ (°)	k_{app} (N/mm)	F_{term} (N)	s_{term} (mm)	θ (°)	k_{app} (N/mm)
0.10	22.0	7.00	53.5	3.14	30.1	9.90	75.6	3.04
0.15	20.0	6.30	48.1	3.17	24.7	7.96	60.8	3.10
0.20	16.3	5.10	39.0	3.20	18.4	5.86	44.8	3.14
0.25	25.5	4.50	34.4	5.67	18.5	3.38	25.8	5.48
0.30	38.0	6.64	50.7	5.72	21.0	3.20	24.4	6.56
0.40	33.5	3.20	24.4	10.47	30.0	4.50	34.4	6.67
0.50	51.1	3.11	23.8	16.43	38.5	2.39	18.3	16.11

where $\Delta R = R_{\max} - R_{\min}$ and ΔF is the common applied force range. Because both specimens used the same ΔF, their sensitivity ratio equals the ratio of their resistance excursions.

Separate low-force sweeps recorded the ESP32-S3 capacitive-channel output and the applied force. The archived analysis applies a square-root mapping to the raw touch count for visualization. We use *observed saturation* descriptively for the point beyond which the mapped output forms a plateau despite continued loading; it is not a calibrated capacitance threshold. The loading branch reached approximately 1 N for C12R1 and 14 N for C1R4. Figure 5 shows the archived force-aligned traces and their different force scales.

4.4 Constant-Load Stability Ratio and Short Bending

Under constant force, we quantify how steady the loaded resistive output is by the ratio of its mean μ to its standard deviation σ, expressed in decibels:

$$S_{\text{dB}} = 20 \log_{10}\left(\frac{\mu}{\sigma}\right). \tag{7}$$

We name this quantity the *stability ratio* rather than an SNR, because it is an inverse coefficient of variation: it is computed from the loaded trace alone and never references an unloaded recording. It therefore measures relative temporal fluctuation under load, not signal against a noise floor. This makes it distinct from the Prototype 2 values in Table 4, which are a true SNR obtained by comparing a 120 s loaded recording against a separately acquired 30 s unloaded noise floor. The two quantities share a unit but are not comparable with one another, and only S_{dB} enters the geometry selection reported below. For clamp conditions XC3, XC5, and XC7, S_{dB} was 50.73, 52.19, and 52.34 dB for C1R4 and 50.42, 38.34, and 44.25 dB for C12R1. The arithmetic means are 51.75 and 44.34 dB, respectively, a 7.42-dB difference. C1R4 varies by only 1.61 dB across those labels. We use clamp identifiers because the nominal force assigned to XC5 is inconsistent across the measurement tables.

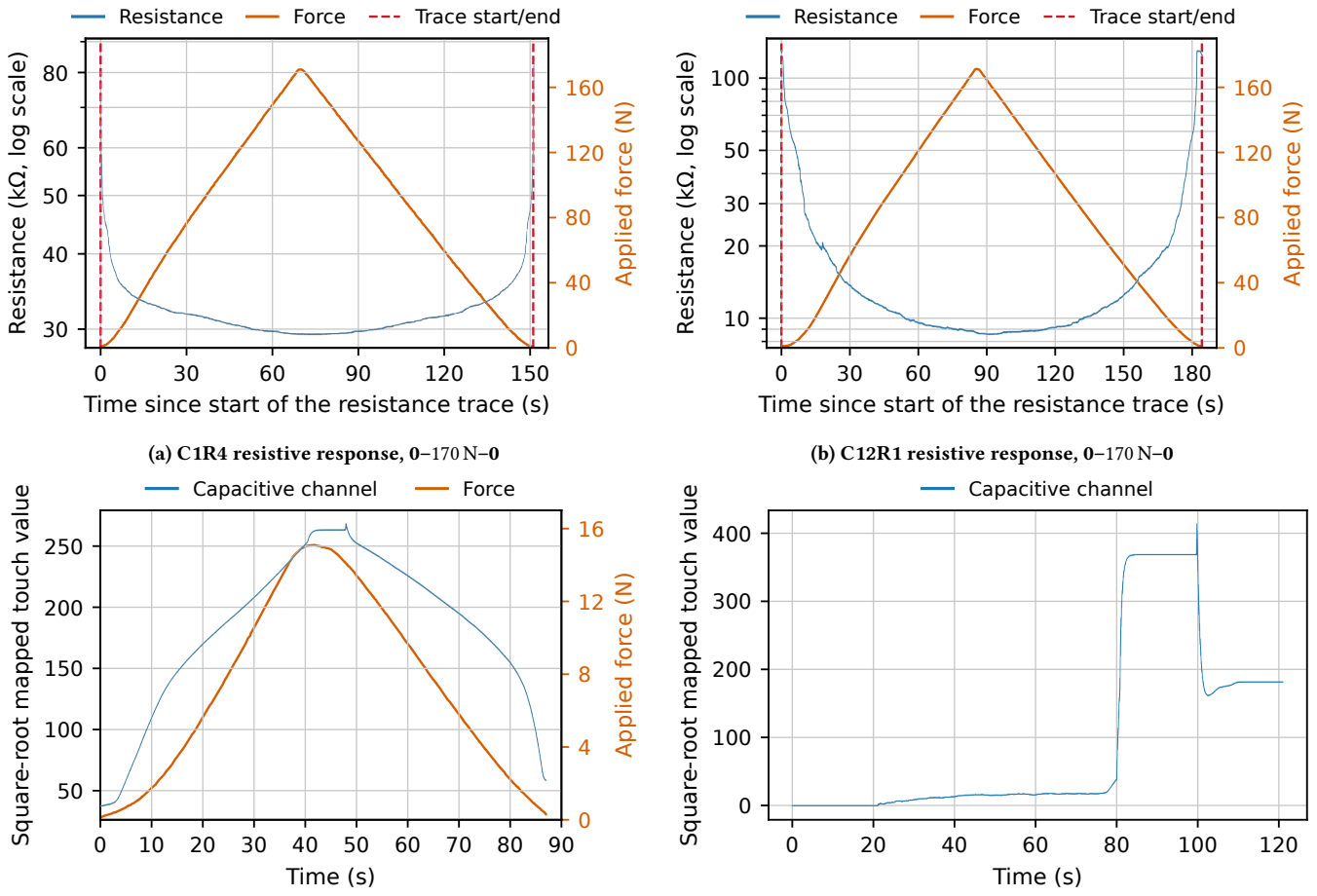
Each baseline and post-exposure resistance trace was acquired during a triangular compression ramp from nominally zero load to approximately 170 N and back to zero using the universal testing machine. The horizontal axis in Figure 6 represents elapsed time over this loading and unloading sequence; the ramp speed was not preserved in the archive. For short-bending assessment, a baseline trace was followed by a 10-min bending exposure, a 10-min recovery interval, and a repeated trace. The sequence was performed twice. Displacement was 4 mm for C1R4 and 3.5 mm for C12R1. Bending frequency and cycle count were not recorded. We compare the minimum resistance, whole-curve normalized root-mean-square error (NRMSE), and reported sensitivity retention, but call the experiment *short-cycle electrical stability*, not durability.

5 Results

5.1 Electrical Response and Bending Stability

Table 6 consolidates the key electrical metrics. The clamp measurement has the larger excursion for C12R1. The constant-load and post-bending measurements show the more stable pattern for C1R4. After the first and second bending exposures, C1R4's pressure–resistance curve minimum changed from 29.44 to 30.26 and 30.61 kΩ, corresponding to changes of 2.8% and 4.0%. C12R1 changed from 8.61 to 33.64 and 43.99 kΩ, corresponding to 290.6% and 410.7%. These pressure–resistance sweeps were recorded on separately fabricated 0.2 mm specimens under a triangular compression profile, not the standing body-weight condition of Table 2; their absolute resistance levels therefore differ from the screening R_0 and R_{body} values, consistent with the large unit-to-unit variation typical of Velostat [Giovanelli and Farella 2016], so only the within-experiment change across the two exposures is compared here. The two exposures also differ in character. C1R4's curve minimum and NRMSE change little between the first and second exposure, indicating an essentially settled response, whereas C12R1 changes sharply after the first exposure and far less after the second. This pattern is consistent with an irreversible rearrangement of the conductive network that settles toward a new equilibrium instead of degrading without bound. We still report it as short-cycle behavior and not as fatigue life, because only two exposures were performed and the cycle count within each exposure was not recorded. Figure 6 shows the underlying traces and makes the contrast directly visible: the three C1R4 curves lie almost on top of one another, whereas C12R1's baseline sits far below its two post-bending curves across the whole load range.

Whole-curve NRMSE for C1R4 was 5.12% after exposure one and 4.73% after exposure two, compared with 41.19% and 46.12% for C12R1. Sensitivity retention was 110.2% then 91.9% for C1R4 and 74.8% then 63.6% for C12R1. The C1R4 value above 100 % after the first exposure indicates a small transient rise in force sensitivity,



(a) C1R4 resistive response, 0–170 N–0

(b) C12R1 resistive response, 0–170 N–0

(c) C1R4 mapped capacitive response to ≈ 14 N

(d) C12R1 mapped capacitive response to ≈ 1 N

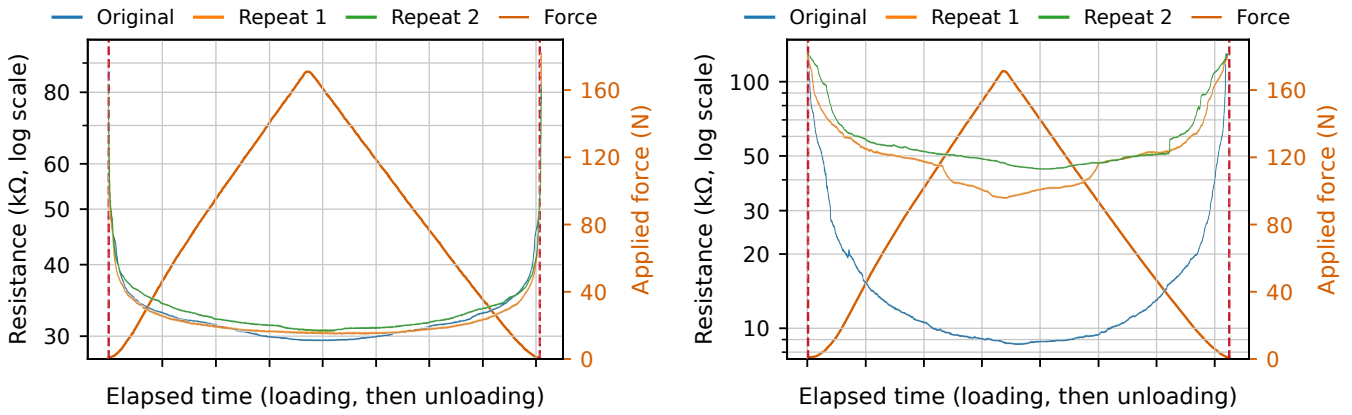
Figure 5: Pressure response of the two assembled prototype configurations, from the archived recordings. Orange: force ramp of the testing machine (right axis). (a, b) Resistance over the triangular ramp; C12R1 has the larger excursion. (c, d) Square-root mapped capacitive-channel output from separate low-force sweeps; C12R1 plateaus earlier, and no force trace was archived for (d). Axes differ between panels, and the capacitive values are not calibrated.

Table 6: Electrical response and short-bending stability of C1R4 and C12R1.

Metric	C1R4	C12R1
Circle / ring width (mm)	1 / 4	12 / 1
Unloaded resistance (kΩ)	20.0	9.0
XC7-clamp resistance (kΩ)	13.0	1.3
XC7-clamp reduction (%)	35.0	85.6
Mean stability ratio S_{dB} across XC3/XC5/XC7 (dB)	51.75	44.34
Curve-minimum change after exposure 2 (%)	4.0	410.7
Second-exposure NRMSE (%)	4.73	46.12
Second-exposure sensitivity retention (%)	91.9	63.6

followed by a value below 100 % after the second exposure. This is consistent with, but does not establish, the conductive-network rearrangement proposed above. C12R1 is not a failed geometry, but its larger clamp response comes with less stable behavior. Across the electrical and bending criteria, we selected C1R4 for the six-zone implementation.

Pressure response of the two channels. The assembled prototypes also differ in pressure response (Figure 5). Across the common 0–170 N resistive loading range, C12R1 has a 2.7× larger resistance excursion and therefore a 2.7× higher mean force sensitivity by Equation (6). Its resistance continues to decline across the loading branch, whereas C1R4 changes most strongly at low load and then flattens. On the mapped capacitive channel, C12R1 reaches an observed plateau within the low-force C12R1 sweep, whereas C1R4 varies over a wider force interval before flattening near the upper end of its approximately 14 N sweep. These prototype-level results support different useful ranges, but the comparison includes the different Velostat stacks documented in the method and does not establish a geometry-only law or calibrated pressure resolution.



(a) C1R4: three nearly coincident curves

(b) C12R1: baseline far below both post-bending curves

Figure 6: Pressure–resistance traces before and after the two bending exposures (log resistance; the horizontal axis is elapsed time over a triangular load ramp to ≈ 170 N and back, so each curve is traversed left to right as load rises and then falls). Repeat 1 and Repeat 2 follow the first and second exposure. Orange: force ramp. C1R4 (a) returns three nearly coincident curves (NRMSE 5.12% and 4.73%), whereas C12R1 (b) shifts by roughly a factor of four after the first exposure and does not recover (NRMSE 41.19% and 46.12%). Note the different vertical ranges.

Because the six-zone stack must commit to a single printed geometry, we retain C1R4 for its greater short-cycle stability and simpler assembled stack; a mixed-geometry insole is left to future work.

5.2 Six-Zone System Results

Tests 3 and 4 use the galvanically separated C1R4 stack and span 69.85 and 31.08 s, respectively. Both sessions maintain exact resistive/capacitive alternation with zero within-stream sequence gaps, and the measured per-mode rate is 25.0 Hz, matching the nominal firmware schedule.

Figure 7 shows Test 4 without converting raw counts to pressure. All six capacitive channels vary over the recording after per-channel visualization normalization. On the resistive side, all six sites respond to loading. Five of them (S1–S4 and S6) change state synchronously, so their majority state serves as an internal load indicator; conditioned on it, the sixth channel S5 separates cleanly, with a median of 857 counts unloaded against 0 counts loaded in Test 3. This is a relative, within-recording classification: no synchronized force reference exists, so it establishes that the sites transduce, not what pressure they report.

What differs between sites is not whether they respond but where their working range falls relative to the fixed divider, and the two ends of the ADC range are not affected equally. Table 9 therefore reports clipping at both rails. In Test 4, S1, S2, S4, and S6

Table 7: Prototype generations compared on channel-integration outcomes. Resistive channels are counted twice: those that respond to load at all, and those with a design-conforming baseline that keeps them predominantly inside the ADC window; the exact rail fractions are reported separately. "Usable C channels" counts capacitive channels that produced varying data. Fractions are over implemented channels. In Prototype 4 all six sites transduce, but only S3 combines that with a design-conforming baseline (Tables 9 and 8).

Feature	P1	P2	P3	P4
Electrode design	Parallel	Circular	R–C	R–C
Shared-conductor failure observed	no	no	**yes**	no
Capacitive froze	–	–	**yes**	no
R channels responding to load	1/1	1/1	0/1	6/6
R channels inside the ADC window	1/1	1/1	0/1	1/6
Usable C channels	1/1	1/1	0/1	6/6

Table 8: Per-site resistive working point in the two Prototype 4 recordings, recomputed from the archived recordings. R_{unl} and R_{load} are median resistances in the unloaded and loaded state, converted from raw counts through Equation (3) with $R_{ref} = 4.7$ kΩ; "> ceil." marks a median above what the divider resolves, "floor" a median at the 0 rail. The load state is the majority state of the five mutually synchronous channels, not a force reference. Capacitive values are raw `touchRead()` counts pooled over all six sites (full range; 2nd–98th percentile in brackets).

Test 3	S1	S2	S3	S4	S5	S6
R_{unl} (kΩ)	> ceil.	> ceil.	16.7	> ceil.	1.2	> ceil.
R_{load} (kΩ)	0.31	0.19	0.13	0.20	floor	0.20
Test 4	**S1**	**S2**	**S3**	**S4**	**S5**	**S6**
R_{unl} (kΩ)	> ceil.	> ceil.	17.5	> ceil.	0.50	> ceil.
R_{load} (kΩ)	0.44	0.19	0.12	floor	floor	0.24

Test	Date	Capacitive S1–S6 (raw counts)	
3	2026-06-19	46 383–189 306	[47 780–183 439]
4	2026-06-22	51 962–132 672	[68 650–123 879]

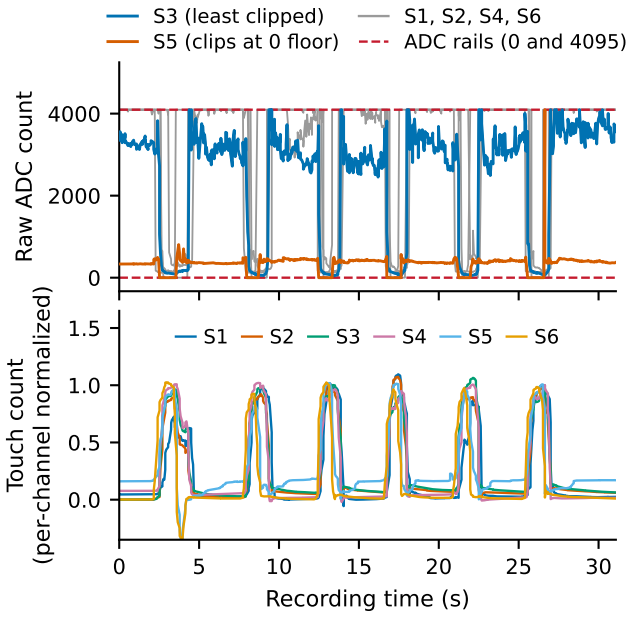


Figure 7: Raw six-zone Test 4 recording. Top: the resistive channels, with both ADC rails marked. S1, S2, S4, and S6 (grey) spend most of the session at the 4095 ceiling and drop away from it only while loaded; S3 remains inside the window for 96.8% of samples; S5 sits an order of magnitude lower and clips at the 0 floor during the same events. Bottom: six varying capacitive channels, normalized per channel by the 2nd and 98th percentiles. No synchronized force ground truth is available; the six loading events are inferred from the synchronous state changes of the channels themselves.

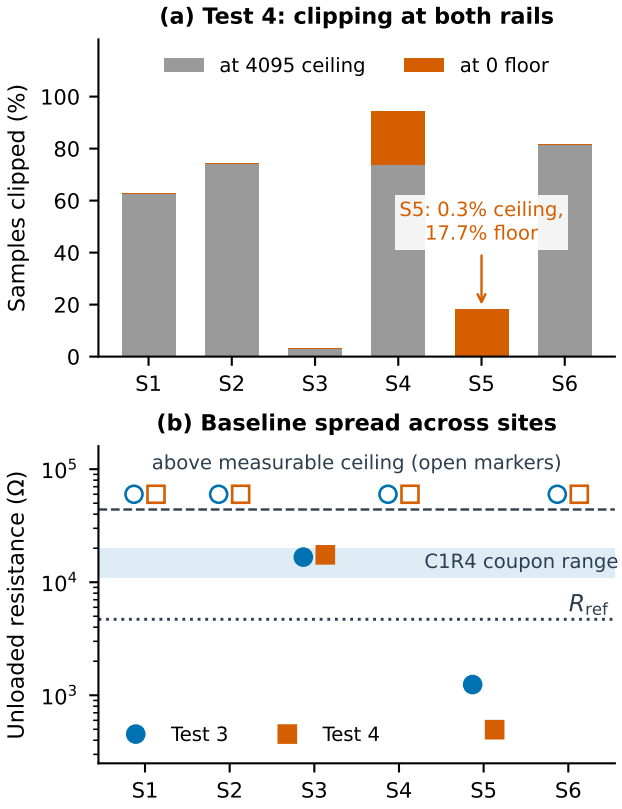


Figure 8: Per-site working point in the six-zone recordings. (a) Clipping at both ends of the 12-bit range in Test 4: S5 reaches the 4095 ceiling in only 0.3% of samples but clips at the 0 floor in 17.7%; S4 clips at both rails. (b) Unloaded resistance per site (log scale; open markers denote medians above what the 4.7 kΩ divider resolves). Only S3 falls inside the C1R4 coupon interval of Table 2; S5 sits more than an order of magnitude below it. Across six nominally identical printed sites of one insole, the baseline spans more than two orders of magnitude.

sit at the 4095 ceiling for 62.8–81.6% of their samples, whereas S5 reaches the ceiling in only 0.3% of samples but spends 17.7% at the 0 floor, and 40.1% in Test 3; S4 clips at both ends. Counting only the ceiling would therefore identify S5 as the one unaffected channel, when it is in fact the one channel that clips at the opposite rail.

Table 8 makes the cause explicit by giving each site's median resistance in the unloaded and loaded state. Four sites (S1, S2, S4, S6) have an unloaded resistance above what the 4.7 kΩ divider resolves. S3 sits at 16.7 and 17.5 kΩ in the two sessions, inside the 11 kΩ to 20 kΩ interval measured on C1R4 coupons (Table 2), and it stays within the ADC window for 87.2% and 96.8% of its samples, which makes it the least clipped channel in both recordings. S5, by contrast, has an unloaded resistance of 1.2 and 0.50 kΩ, more than an order of magnitude below both S3 and the coupon interval. S5 remains readable only because its whole characteristic is shifted downward, and it pays for that by bottoming out under load.

Across six nominally identical printed sites within one device, the unloaded resistance thus spans at least two orders of magnitude, from 0.5 kΩ to beyond the measurable ceiling (Figure 8). This is a fabrication result, not a readout result, and it sharpens the argument of Section 6.3: no single global R_{ref} can serve a hundredfold spread in base resistance, so per-channel matching is a requirement and not a refinement. It also exposes site-to-site variation within one device as a manufacturability limit that the coupon-level screening of Section 5.1 cannot reveal, since it characterizes one specimen at a time. Printed pad quality, solder-joint geometry, and local Velostat contact pressure are the plausible contributors.

The separated topology does not reuse a conductor between the two readouts, and the recorded capacitive streams do not exhibit the frozen output observed with the shared-conductor configuration. Table 7 places these recordings in the context of the four prototype generations: the shared-electrode Prototype 3 produced no usable data on either channel, whereas the galvanically separated Prototype 4 recovers all six capacitive channels and six resistive channels that respond to load, of which one (S3) keeps a design-conforming baseline inside the ADC window. The S5 band also sits at a markedly different level in the two sessions, recorded three days apart. With

Table 9: Clipping of the six resistive channels at *both* ends of the 12-bit range: fraction of samples at the 4095 ceiling and at the 0 floor in the two galvanically separated system recordings. S5 clips at the floor instead of the ceiling; S3 is the least clipped site in both sessions.

Test	Rail	S1	S2	S3	S4	S5	S6
3 (69.85 s)	4095	44.7 %	42.4 %	12.8 %	40.6 %	0.0 %	43.4 %
	0	0.0 %	0.0 %	0.0 %	0.0 %	**40.1 %**	0.0 %
4 (31.08 s)	4095	62.8 %	74.5 %	3.2 %	73.8 %	0.3 %	81.6 %
	0	0.0 %	0.0 %	0.0 %	**20.5 %**	**17.7 %**	0.0 %

no force reference and no configuration metadata linking the sessions, we cannot separate a genuine baseline shift of that site from differences in mounting and contact conditions between recordings; we therefore treat the counts as comparable only within a session, not across sessions. Without a controlled single-zone stimulus and a synchronized force reference, these tests characterize the acquisition pipeline and the per-site working points; they do not quantify crosstalk, localization, or pressure accuracy.

6 Discussion

6.1 Functional Geometry Couples Response and Readout

The ring–circle family illustrates a computational-fabrication principle: functional geometry determines more than external form. Circle diameter and ring width jointly define contact area, gap, and plausible current paths; the measurements associate those candidates with different unloaded resistance, response amplitude, noise, and post-bending behavior. A single response-amplitude objective is insufficient: the C12R1 clamp measurement has the larger excursion, while C1R4 has the higher mean stability ratio, smaller curve-minimum change, and better whole-curve similarity. C12R1 also needed a folded film and a paper interlayer to reach a usable working point with the present divider. The six-zone implementation therefore uses C1R4, favoring measured stability and the simpler stack over the maximum resistive excursion. A fabrication-aware selection has to weigh these criteria together, and the appropriate weighting depends on the application, not on the geometry.

The 20-condition screen identifies manufacturable regions of the parameter space and makes failed solder connections visible. It is not a response-surface optimization: only two candidates receive deeper characterization. Instead, it provides a fabrication-aware basis for selecting geometries against multiple electrical and mechanical objectives.

6.2 Two Observables from One Printed Volume

The two channels are not a redundant pair but a complementary one, and the fabricated stack is what makes the pairing cheap. The coupon measurements show different response ranges. The resistive channel responds over the 0–170 N ramp, while the mapped capacitive output flattens within the separate low-force sweeps (Figure 5). C1R4 varies over a wider capacitive force interval than C12R1. These observations motivate combining the channels, but do not establish a calibrated crossover or their respective roles during gait.

What additive manufacturing contributes is that both observables occupy the same site instead of competing for it. The capacitive electrode is layer 3 of the stack and the resistive circle is layer 5, separated by a single printed dielectric (Table 3); they share one footprint, one load path, and one print run. Achieving the same co-location by assembly would mean either stacking two separately manufactured sensors at each anatomical landmark or splitting the available area between them. Area is exactly what the side-by-side forefoot constraint of Section 3.1 does not allow. The dual-mode site is what lets a single 18 mm footprint carry two transduction principles.

The six-zone recordings show that both observables do respond at every site. Conditioned on the load state inferred from the resistive channels, all six capacitive channels separate loaded from unloaded samples in both sessions, with descriptive standardized mean differences between 1.5 and 18.6, computed as the difference in conditional means divided by the average of the two population standard deviations. These within-recording scores are not independent-specimen estimates. Two consequences follow. First, the interleaved scheduler does not trade one modality against the other: the capacitive stream stays responsive while the resistive excitation runs, which is precisely what the shared-conductor Prototype 3 failed to do. Second, and unplanned, the galvanic separation also decouples *fabrication* faults. At S5 the resistive path sits an order of magnitude away from its design resistance, yet the capacitive channel at the same site behaves like the other five. A defect in one printed path therefore need not remove the site from the map, which is a practical argument for dual-mode sites in a device with six hand-soldered sensors and measurable site-to-site variation.

We stop short of claiming a fused estimate. No sensor-fusion algorithm is implemented, the crossover between the two ranges is not calibrated, and the capacitive channel is reported in raw counts, so the complementarity is demonstrated as overlapping responsiveness rather than as a combined pressure reading. Establishing the crossover against a reference load, and deciding whether the two channels are best combined by switching or by weighting, is the obvious next step and does not require changing the printed sensor.

6.3 Readout Working Point

The integrated recordings expose a distinction between sensing topology and readout working point. Electrical isolation removes conductor sharing, but it does not place the resistive channels within the ADC range. Four channels in Test 4 spend most of the session at the upper rail, one reaches it intermittently, and one clips at the lower rail instead, because a single shared reference resistor cannot match six working ranges that differ by two orders of magnitude (Tables 9 and 8). Equation (4) makes this mismatch quantitative. For C1R4 the measured resistance interval runs from $R_{\min} \approx 11\,\mathrm{k\Omega}$ under body-weight load to $R_{\max} = 20\,\mathrm{k\Omega}$ unloaded, so the log-symmetric optimum is $R_{\mathrm{ref}} = \sqrt{R_{\min} R_{\max}} \approx 15\,\mathrm{k\Omega}$, roughly three times the 4.7 kΩ actually installed in the six-zone divider. We deliberately base this estimate on the screening interval, which is the conservative case: the separately fabricated pressure–resistance specimens of Section 5.1 sit at higher absolute resistance (curve

minima near 29 kΩ), so their log-symmetric optimum is higher still and the mismatch against the installed resistor approaches an order of magnitude. With $R_{\text{ref}} \ll R_s$ across the whole working range, Equation (3) holds V_{ADC} near the upper rail, which is consistent with the upper-rail saturation affecting S1, S2, S4, and S6 for most of Test 4; S3 reaches that rail in 3.2% of samples (Table 9). Selecting C1R4 avoids modifying the Velostat stack, but the divider still requires per-channel adjustment. A controlled follow-up should measure R_{min} and R_{max} for every fabricated channel and compare fixed, selected, or digitally switched reference resistors according to Equation (4), while retaining matched force and configuration metadata.

6.4 Implications for Computational Fabrication

For this particular sensor and use case, circle diameter and ring width act as functional fabrication parameters: they set the printed conductor area and separation, and in doing so move the assembled electrical working point. The relevant fabricated object therefore includes the CAD geometry, printed height, pad geometry, Velostat stack, and divider, rather than the printed coupon alone. The system measurements make this coupling concrete: a geometry can remain electrically responsive yet be poorly matched to a fixed divider, and an isolated sensing topology can still produce unusable rail-limited data.

What transfers. Three findings are not specific to feet. The first is geometric separation as a base-resistance control. Non-overlapping electrodes define a lateral current path through the piezoresistive film and provide a design variable for adjusting the electrical working point. The screen in Table 2 characterizes the ring–circle family; it does not quantify a matched-stack advantage over opposing plates. The transferable step is to evaluate electrode separation alongside the assembled resistance range and readout circuit. The second is that the readout working point belongs inside the geometry decision, not after it. Equation (4) ties a geometric choice to a specific resistor value, and the six-zone recordings show that the rule has to be applied per channel once fabrication variance is present, because a single global value cannot serve a hundredfold baseline spread. The third is that fabrication yield belongs in the screen itself. Recording which coupons broke, which were electrically unstable, and which failed at the manual solder joint turns a geometry screen into a manufacturability map instead of a response map, and in this study those outcomes constrained the usable design region as much as the electrical measurements did.

What does not transfer. The numbers do not. The 18 mm outer diameter follows from placing three sensors side by side across the metatarsal region, the six sites follow from clinically established landmarks of the diabetic foot, and the specific ring and circle values that survive the screen follow from those two constraints together with the resistance of this particular Velostat and the resolution of this particular printer. Another application would re-derive all of them. What carries over is the procedure, not the family member that won here: screen a parametric family against electrical response *and* fabrication yield, then match the readout to the measured interval.

Beyond insoles. The constraint that produced this electrode family is not anatomical. It is the combination of a compressible resistive film, a divider with a limited ADC, a force range spanning two orders of magnitude, and a thin flexible package with little area per site. That combination recurs in robotic gripper and fingertip pads, prosthetic and orthotic liners, seat and mattress pressure mats, and instrumented garments. In each case the lateral-path principle needs only a printable conductor and a compressible resistive layer, and the complementary dual-mode arrangement of Section 6.2 needs only one additional printed dielectric. Conversely, the principle has little to offer where a calibrated absolute pressure at a single point is required, or where area is plentiful enough that an opposing-plate electrode already lands inside the readout range.

A design response to the failures reported here. The fabrication problems documented above have since shaped a revised sensor that we describe as a design rationale rather than as a characterized result, since it is not part of the evaluation reported in this paper. In that revision the manually inserted film is replaced by an integrated build in which each site carries its own Velostat pad, deliberately oversized relative to its electrode pair. Oversizing each pad is intended to maintain coverage of both electrodes despite lateral placement variation. Its effect on contact conditions and site-to-site resistance variation remains unmeasured. Separate pads avoid introducing a continuous conductive film between sites; isolation between resistive and capacitive conductors within each site remains a separate requirement, as the Prototype 3 failure demonstrated. Whether this narrows the site-to-site spread reported in Section 5.2 is an empirical question we have not yet answered.

A stronger computational model would require replicated geometry batches. Each coupon should therefore be linked to its CAD, print run, assembly, and readout configuration; matched force records can then separate circle diameter, ring width, and fabrication variation. Only then would the data support a response surface or multi-objective geometry selection.

6.5 Toward Clinical Integration

The shared-conductor failure of Prototype 3 shows that electrode-topology choices have system-level consequences already at the prototype stage: a stack that works as one isolated sensor can couple two readouts once six sites share a conductor. Removing that failure in Prototype 4 is a prerequisite for continuous, multi-site plantar monitoring [Hochlenert 2024; Matijevich et al. 2024]. Several steps remain before clinical use: per-channel reference-resistor matching to remove the ADC saturation observed here, pressure calibration against a reference load cell, and validation under dynamic gait rather than static clamping. These are engineering and study-design tasks rather than changes to the printed sensor, which supports the feasibility of the additively manufactured, dual-mode approach for insole integration [Samarentsis et al. 2022].

7 Limitations

The geometry–height series used one specimen per condition, and actual laminate thickness was not recorded. We therefore use these measurements for specimen-level comparison and design selection rather than as material-property estimates. Independent specimen identity was not tracked consistently across the focused electrical

tests. The reported differences therefore describe C1R4 and C12R1 as fabricated in this study; replicated print runs are required to estimate independent effects of circle diameter and ring width.

The short-bending protocol was limited to two 10-min exposures, and cycle count was not recorded. It therefore characterizes short-cycle electrical stability, not fatigue or long-term durability. What those two exposures already produced is nevertheless relevant to continuous use. C12R1's pressure–resistance curve minimum moved by 410.7% and its whole-curve NRMSE reached 46.12% after the second exposure, whereas C1R4 stayed at 4.0% and 4.73%. Two bending events are far fewer than a single day of walking. C1R4's near-coincident curves show that a settled response is achievable in this material system, and the small difference between its first and second exposure suggests a response that settles rather than drifting without bound; neither observation establishes that it stays settled over thousands of cycles, and we cannot exclude that a comparable rearrangement eventually appears in C1R4 as well. An insole intended for continuous wear therefore requires a cyclic endurance test with a recorded cycle count and periodic recalibration checks. We have not performed one, so durability, one of the challenges cited as motivation in Section 1, remains open for this design.

The six-zone recordings expose a large site-to-site spread in unloaded resistance within a single device, but they do not explain it: printed pad quality, solder-joint geometry, and local Velostat contact pressure were not measured per site, and only two sessions on one insole are available. The spread is therefore reported as an observed manufacturability limit, not as a characterized fabrication mechanism.

Neither sensing mode is calibrated to absolute pressure, and the capacitive count in particular is reported in raw units. The six-zone recordings have no synchronized force or location ground truth; they demonstrate acquisition behavior and expose ADC saturation but do not establish pressure accuracy, localization, or clinical performance. Absolute-pressure calibration of both channels, and controlled single-zone stimulation to quantify crosstalk and localization, remain future work.

8 Conclusion & Future Work

We presented a 20-member geometry-defined current-path design space for inkjet-printed resistive-capacitive sensors. The measurements contrasted the C12R1 configuration's larger XC7-clamp response with the C1R4 configuration's 7.42-dB higher mean constant-load stability ratio and much smaller post-bending curve-minimum change. Because C12R1 needed a folded-film and paper stack to reach a useful working point with the present divider while C1R4 did not, that contrast belongs to the two assembled configurations rather than to electrode geometry in isolation; separating the two requires a matched stack at replicated specimen counts, which we identify as the single most valuable follow-up. Tests across a range of nominal printed heights documented fabrication constraints. Across the electrical and bending criteria, we selected C1R4 for an insole system with six electrodes. Two system recordings showed uninterrupted interleaved acquisition and identified resistive channels clipped against both ADC rails by an unmatched fixed reference resistor, with unloaded site resistances spanning more than two orders of magnitude within one device. Electrode geometry, printed structure, assembled stack, and readout working point therefore require joint evaluation.

Establishing how sensor geometry affects performance requires raw data from replicated, identically fabricated specimens. Our immediate next steps are to match each channel's reference resistor to bring all resistive signals into a readable range, calibrate both sensing modes against a reference load, and test the system during walking; none of these steps requires modifying the printed sensor design. Overall, these findings support treating printed geometry as a first-class design variable for dual-mode plantar pressure sensing, and show concretely why sensor layout has to be co-designed with the readout hardware rather than optimized before it. Future clinical evaluation will require pressure calibration, durability testing, and appropriate ethics approval before studies with patients.

8.1 Data and Artifact Availability

Available research artifacts are provided at https://github.com/susesKaninchen/glucosole-scf2026-artifacts. The repository contains archived acquisition firmware, a Python/Tkinter recorder, four raw system recordings, geometry-screening table values, analysis scripts, and archived figures. The historical Java GUI source, original electrode CAD and print-job files, and original force-response recordings are not currently included; the repository lists these missing materials explicitly. The available scripts reproduce the system-recording analyses and selected figures, not every fabrication and characterization result. Reuse is governed by the repository's non-commercial research license; other uses require permission.

Acknowledgments

This work was supported by the Federal Ministry of Research, Technology and Space of Germany under grant number 03DPC0711A.

9 Ethics and Privacy Statement

The sensors developed in this work are intended to support future research on non-invasive monitoring of plantar pressure for people with diabetes mellitus. No recruited participant study was conducted. A member of the research team applied body weight as a single mechanical loading condition for the screening measurement in Table 2; no behavioral, clinical, or personally identifiable data were collected. Future clinical validation studies will require appropriate ethics approval in line with the ACM Publications Policy on Research Involving Human Participants and Subjects [ACM Publications Board 2021]. The developed technology bears no foreseeable risk of misuse beyond standard considerations for wearable medical devices.

References

Abdul Hadi Abdul Razak, Aladin Zayegh, Rezaul K. Begg, and Yufridin Wahab. 2012. Foot Plantar Pressure Measurement System: A Review. *Sensors* 12, 7 (2012), 9884–9912. doi:10.3390/s120709884

ACM Publications Board. 2021. ACM Publications Policy on Research Involving Human Participants and Subjects. Accessed: January 2026. https://www.acm.org/publications/policies/research-involving-human-participants-and-subjects

Pablo Aqueveque, Rodrigo Osorio, Francisco Pastene, Francisco Saavedra, and Esteban Pino. 2018. Capacitive Sensors Array for Plantar Pressure Measurement Insole Fabricated with Flexible PCB. In *2018 40th Annual International Conference of the IEEE Engineering in Medicine and Biology Society (EMBC)*. IEEE, Piscataway, NJ, USA, 4393–4396. doi:10.1109/EMBC.2018.8513383

David G. Armstrong, Tze-Woei Tan, Andrew J. M. Boulton, and Sicco A. Bus. 2023. Diabetic Foot Ulcers: A Review. *JAMA* 330, 1 (2023), 62–75. doi:10.1001/jama.2023.10578

S Sandra Bae, Takanori Fujiwara, Danielle Szafir, Ellen Yi-Luen Do, and Michael L Rivera. 2025. Computational Design and Single-Wire Sensing of 3D Printed Objects with Integrated Capacitive Touchpoints. In *Proceedings of the ACM Symposium on Computational Fabrication*. Association for Computing Machinery, New York, NY, USA, 1–19. doi:10.1145/3745778.3766650

Bessey GmbH & Co. KG. 2022. *Clippix XC7 – Klemmzange: Produktdatenblatt*. Accessed: January 2026. https://www.bessey.de/de-DE/Produkte/Spanner/Clippix-XC-Klemme/Clippix-XC7

Sicco A. Bus and Jaap J. van Netten. 2016. A shift in priority in diabetic foot care and research: 75 % of foot ulcers are preventable. *Diabetes/Metabolism Research and Reviews* 32, Suppl 1 (2016), 195–200. doi:10.1002/dmrr.2738

Pedro Castro-Martins, Arcelina Marques, Luís Coelho, Mário Vaz, and João Santos Baptista. 2024. In-shoe plantar pressure measurement technologies for the diabetic foot: A systematic review. *Heliyon* 10 (2024), e29672. doi:10.1016/j.heliyon.2024.e29672

Andrius Dzedzickis, Ernestas Sutinys, Vytautas Bucinskas, Urte Samukaite-Bubniene, Baltramiejus Jakstys, Arunas Ramanavicius, and Inga Morkvenaite-Vilkonciene. 2020. Polyethylene-Carbon Composite (Velostat®) Based Tactile Sensor. *Polymers* 12, 12 (2020), 2905. doi:10.3390/polym12122905

M. Fernando, R. Crowther, P. Lazzarini, K. Sangla, M. Cunningham, P. Buttner, and J. Golledge. 2013. Biomechanical characteristics of peripheral diabetic neuropathy: a systematic review and meta-analysis of findings from the gait cycle, muscle activity and dynamic barefoot plantar pressure. *Clinical Biomechanics* 28, 8 (2013), 831–845. doi:10.1016/j.clinbiomech.2013.08.004

F. G. R. Fowkes, D. Rudan, I. Rudan, V. Aboyans, J. O. Denenberg, M. M. McDermott, P. E. Norman, U. K. A. Sampson, L. J. Williams, G. A. Mensah, and M. H. Criqui. 2013. Comparison of global estimates of prevalence and risk factors for peripheral artery disease in 2000 and 2010. *The Lancet* 382, 9901 (2013), 1329–1340. doi:10.1016/S0140-6736(13)61249-0

Marco Torge Gabrecht, Hengyu Wang, and Denys Jörg Christian Matthies. 2023. PneuShoe: a pneumatic smart shoe for activity recognition, terrain identification, and weight estimation. In *Proceedings of the 8th International Workshop on Sensor-Based Activity Recognition and Artificial Intelligence*. Association for Computing Machinery, New York, NY, USA, 1–5. doi:10.1145/3615834.3615853

Galdabini S.p.A. 2021. *Quasar 100 Universal Testing Machine: Technical Data Sheet and User Manual*. Accessed: January 2026. https://www.galdabini.it/en/product/quasar/

Davide Giovanelli and Elisabetta Farella. 2016. Force Sensing Resistor and Evaluation of Technology for Wearable Body Pressure Sensing. *Journal of Sensors* 2016 (2016), 1–13. doi:10.1155/2016/9391850

Tobias Grosse-Puppendahl, Christian Holz, Gabe Cohn, Raphael Wimmer, Oskar Bechtold, Steve Hodges, Matthew S Reynolds, and Joshua R Smith. 2017. Finding common ground: A survey of capacitive sensing in human-computer interaction. In *Proceedings of the 2017 CHI Conference on Human Factors in Computing Systems*. Association for Computing Machinery, New York, NY, USA, 3293–3315. doi:10.1145/3025453.3025808

Kazune Hagino, Daisuke Iwai, and Kosuke Sato. 2017. Place Management of Electrodes for Embedding Capacitive Multi-touch Sensor on 3D Printed Surfaces. In *Proceedings of the 1st Annual ACM Symposium on Computational Fabrication*. ACM, New York, NY, USA, 1–2. doi:10.1145/3083157.3092889

Dirk Hochlenert. 2024. Sensorassistierte Wundtherapie (SAWT) beim diabetischen Fuß und in der Prophylaxe. *Die Diabetologie* 20 (2024), 72–79. doi:10.1007/s11428-023-01122-4

M. Kalantari, J. Dargahi, J. Kövecses, M. G. Mardasi, and S. Nouri. 2012. A New Approach for Modeling Piezoresistive Force Sensors Based on Semiconductive Polymer Composites. *IEEE/ASME Transactions on Mechatronics* 17, 3 (2012), 572–581. doi:10.1109/TMECH.2011.2108664

Mohammad Reza Khosravani and Tamara Reinicke. 2020. 3D-printed sensors: Current progress and future challenges. *Sensors and Actuators A: Physical* 305 (2020), 111916. doi:10.1016/j.sna.2020.111916

Abdo-Rahmane Anas Laaraibi, Gurvan Jodin, Damien Hoareau, Nicolas Bideau, and Florence Razan. 2023. Flexible Dynamic Pressure Sensor for Insole Based on Inverse Viscoelastic Model. *IEEE Sensors Journal* 23, 7 (2023), 7634–7643. doi:10.1109/JSEN.2023.3245822

Bastian Latsch, Felix Herbst, Mark Suppelt, Julian Seiler, Stephan Schaumann, Sven Suppelt, Alexander A. Altmann, Martin Grimmer, and Mario Kupnik. 2026. Sensor Insoles: A Review. *IEEE Sensors Journal* 26, 3 (2026), 3577–3596. doi:10.1109/JSEN.2025.3638124

Joris J. Laureto, Jerome Tomasi, John A. King, and Joshua M. Pearce. 2017. Thermal properties of 3-D printed polylactic acid–metal composites. *Cogent Engineering* 4, 1 (2017), 1356720. doi:10.1080/23311916.2017.1356720

Arnaldo G. Leal-Junior, Camilo R. Díaz, Carlos Marques, Maria José Pontes, and Anselmo Frizera. 2019. 3D-printed POF insole: Development and applications of a low-cost, highly customizable device for plantar pressure and ground reaction forces monitoring. *Optics & Laser Technology* 116 (2019), 256–264. doi:10.1016/j.optlastec.2019.03.035

Emily Matijevich, Evan Minty, Emily Bray, Courtney Bachus, Maryam Hajizadeh, and Brock Liden. 2024. A Multi-Faceted Digital Health Solution for Monitoring and Managing Diabetic Foot Ulcer Risk: A Case Series. *Sensors* 24, 9 (2024), 2675. doi:10.3390/s24092675

Denys JC Matthies, Maximilian Kasbohm, Gerald Bieber, and Troy Nachtigall. 2025. Technical Analysis for Electro-Sensory 3D Foot Scanning in a Shoe. In *Proceedings of the 18th ACM International Conference on PErvasive Technologies Related to Assistive Environments*. Association for Computing Machinery, New York, NY, USA, 255–264. doi:10.1145/3733155.3733210

Denys JC Matthies, Franz Müller, Christoph Anthes, and Dieter Kranzlmüller. 2013. ShoeSoleSense: proof of concept for a wearable foot interface for virtual and real environments. In *Proceedings of the 19th ACM Symposium on Virtual Reality Software and Technology*. Association for Computing Machinery, New York, NY, USA, 93–96. doi:10.1145/2503713.2503740

S. Morbach, E. Müller, H. Reike, A. Risse, G. Rümenapf, and M. Spraul. 2022. Diagnostik, Therapie, Verlaufskontrolle und Prävention des diabetischen Fußsyndroms. *Diabetologie und Stoffwechsel* 17, S 02 (2022), S186–S218. doi:10.1055/a-1896-4770

Shun Peng, Zhenshuai Wan, Yu Fu, Chong Liu, Ye Tian, Ronghan Wei, Yibin Fan, and Peifang Xin. 2025. Flexible magnetic tactile sensors: Materials, working principles, and applications—A review. *Materials Today Physics* 59 (2025), 101926. doi:10.1016/j.mtphys.2025.101926

Julian Rasch, Florian Müller, Thomas Kosch, Martin Schmitz, and Sebastian S Feger. 2023. Hands-On 3D Printed Electronics. In *Proceedings of the Seventeenth International Conference on Tangible, Embedded, and Embodied Interaction*. Association for Computing Machinery, New York, NY, USA, 1–2. doi:10.1145/3569009.3571846

Pouya Saeedi et al. 2019. Global and regional diabetes prevalence estimates for 2019 and projections for 2030 and 2045: Results from the International Diabetes Federation Diabetes Atlas. *Diabetes Research and Clinical Practice* 157 (2019), 107843. doi:10.1016/j.diabres.2019.107843

Anastasios G. Samarentsis, Georgios Makris, Sofia Spinthaki, Georgios Christodoulakis, Manolis Tsiknakis, and Alexandros K. Pantazis. 2022. A 3D-Printed Capacitive Smart Insole for Plantar Pressure Monitoring. *Sensors* 22, 24 (2022), 9725. doi:10.3390/s22249725

Martin Schmitz, Mohammadreza Khalilbeigi, Matthias Balwierz, Roman Lissermann, Max Mühlhäuser, and Jürgen Steimle. 2015. Capricate: A Fabrication Pipeline to Design and 3D Print Capacitive Touch Sensors for Interactive Objects. In *Proceedings of the 28th Annual ACM Symposium on User Interface Software and Technology*. ACM, New York, NY, USA, 253–258. doi:10.1145/2807442.2807503

Martin Schmitz, Jürgen Steimle, Jochen Huber, Niloofar Dezfuli, and Max Mühlhäuser. 2017. Flexibles: deformation-aware 3D-printed tangibles for capacitive touchscreens. In *Proceedings of the 2017 CHI Conference on Human Factors in Computing Systems*. Association for Computing Machinery, New York, NY, USA, 1001–1014. doi:10.1145/3025453.3025663

Zhiran Shen, Chengduan Yang, Chuanjie Yao, Ziqi Liu, Xinshuo Huang, Zhengjie Liu, Jingshan Mo, Huihua Xu, Gen He, Jun Tao, Xi Xie, Tian Hang, Hui-Jiuan Chen, and Fanmao Liu. 2023. Capacitive–piezoresistive hybrid flexible pressure sensor based on conductive micropillar arrays with high sensitivity over a wide dynamic range. *Materials Horizons* 10 (2023), 499–511. doi:10.1039/d2mh00892k

Pitchaya Sitthi-Amorn, Javier E. Ramos, Yuwang Wang, Joyce Kwan, Justin Lan, Wenshou Wang, and Wojciech Matusik. 2015. MultiFab: A Machine Vision Assisted Platform for Multi-material 3D Printing. *ACM Transactions on Graphics* 34, 4 (2015), 129:1–129:11. doi:10.1145/2766962

Hong Wei Tan, Yu Ying Clarrisa Choong, Che Nan Kuo, Hong Yee Low, and Chee Kai Chua. 2022. 3D printed electronics: Processes, materials and future trends. *Progress in Materials Science* 127 (2022), 100945. doi:10.1016/j.pmatsci.2022.100945

Juan Tao, Ming Dong, Li Li, Chunfeng Wang, Jing Li, Yue Liu, Rongrong Bao, and Caofeng Pan. 2020. Real-time pressure mapping smart insole system based on a controllable vertical pore dielectric layer. *Microsystems & Nanoengineering* 6 (2020), 62. doi:10.1038/s41378-020-0171-1

Panagiotis V. Tsaklis and Nikolaos Tentolouris. 2018. Biomechanics of the Diabetic Foot: The Road to Foot Ulceration. In *The Diabetic Foot*, Aristidis Veves, John M. Giurini, and Robert J. Guzman (Eds.). Springer International Publishing, Cham, 199–215. doi:10.1007/978-3-319-89869-8_12

Tatyana Vasilevitsky and Amit Zoran. 2016. Steel-Sense: Integrating Machine Elements with Sensors by Additive Manufacturing. In *Proceedings of the 2016 CHI Conference on Human Factors in Computing Systems*. ACM, New York, NY, USA, 5731–5742. doi:10.1145/2858036.2858309

Charles Wade, Devon Beck, and Robert MacCurdy. 2025. Implicit Modeling for 3D-printed Multi-material Computational Object Design via Python. In *Proceedings of the ACM Symposium on Computational Fabrication*. Association for Computing Machinery, New York, NY, USA, 1–16. doi:10.1145/3745778.3766659

Hagen Watschke, Marijn Goutier, Julius Heubach, Thomas Vietor, Kay Leichsenring, and Markus Böl. 2021. Novel Resistive Sensor Design Utilizing the Geometric Freedom of Additive Manufacturing. *Applied Sciences* 11, 1 (2021), 113. doi:10.3390/app11010113

Yuan Xiao, Xianjun Wu, Leipeng Yang, and Jiapei Zhu. 2026. Fabrication of high-performance fabric-based capacitive pressure sensors with two-scale synergistic resistive/capacitive hybrid response. *Journal of Materials Science & Technology* 240

(2026), 87–97. doi:10.1016/j.jmst.2025.02.085
Jiakun Yu, Praneeth Bimsara Perera, Rahal Viddusha Perera, Mohammad Mirkhalaf Valashani, and Anusha Withana. 2024. Fabricating Customizable 3-D Printed Pressure Sensors by Tuning Infill Characteristics. *IEEE Sensors Journal* 24, 6 (2024), 7604–7613. doi:10.1109/JSEN.2024.3358330